CrossMark

Intriguing Plasma Composition Pattern in a Solar Active Region: A Result of Nonresonant Alfvén Waves?

Teodora Mihailescu[1] ⓘ, David H. Brooks[2] ⓘ, J. Martin Laming[3] ⓘ, Deborah Baker[1] ⓘ, Lucie M. Green[1] ⓘ,
Alexander W. James[1] ⓘ, David M. Long[4] ⓘ, Lidia van Driel-Gesztelyi[1,5,6] ⓘ, and Marco Stangalini[7] ⓘ

[1] Mullard Space Science Laboratory, University College London, Holmbury St Mary, Dorking, Surrey RH5 6NT, UK; teodora.mihailescu.19@ucl.ac.uk
[2] College of Science, George Mason University, 4400 University Drive, Fairfax, VA 22030, USA
[3] Space Science Division, Naval Research Laboratory, Code 7684, Washington, DC 20375, USA
[4] Astrophysics Research Centre, Queen's University Belfast, University Road, Belfast BT7 1NN, UK
[5] LESIA, Observatoire de Paris, Université PSL, CNRS, Sorbonne Université, Univ. Paris Diderot, 5 place Jules Janssen, F-92195 Meudon, France
[6] Konkoly Observatory, Research Centre for Astronomy and Earth Sciences, Konkoly Thege út 15–17, H-1121, Budapest, Hungary
[7] ASI Italian Space Agency, Via del Politecnico, s.n.c I-00133 Roma, Italy

Abstract

The plasma composition of the solar corona is different from that of the solar photosphere. Elements that have a low first ionization potential (FIP) are preferentially transported to the corona and therefore show enhanced abundances in the corona compared to the photosphere. The level of enhancement is measured using the FIP bias parameter. In this work, we use data from the EUV Imaging Spectrometer on Hinode to study the plasma composition in an active region following an episode of significant new flux emergence into the preexisting magnetic environment of the active region. We use two FIP bias diagnostics: Si X 258.375 Å/S X 264.233 Å (temperature of approximately 1.5 MK) and Ca XIV 193.874 Å/Ar XIV 194.396 Å (temperature of approximately 4 MK). We observe slightly higher FIP bias values with the Ca/Ar diagnostic than Si/S in the newly emerging loops, and this pattern is much stronger in the preexisting loops (those that had been formed before the flux emergence). This result can be interpreted in the context of the ponderomotive force model, which proposes that the plasma fractionation is generally driven by Alfvén waves. Model simulations predict this difference between diagnostics using simple assumptions about the wave properties, particularly that the fractionation is driven by resonant/nonresonant waves in the emerging/preexisting loops. We propose that this results in the different fractionation patterns observed in these two sets of loops.

Unified Astronomy Thesaurus concepts: Solar active regions (1974); Solar abundances (1474)

1. Introduction

One of the major open questions in solar physics is why the elemental composition of some regions in the solar corona is different from that of the underlying photosphere. The relative abundance of different elements is spatially homogeneous in the photosphere (Asplund et al. 2009), but varies in the corona, with a strong dependence on the first ionization potential (FIP) of the element (Meyer 1985). The abundances of elements with a low FIP (<10 eV) are often enhanced in the corona, while the abundances of high-FIP elements (>10 eV) appear to be unchanged. This is called the FIP effect. The degree of enhancement of an element is calculated using the FIP bias parameter. In the extreme ultraviolet (EUV), this is measured as the abundance ratio of a low-FIP element to a high-FIP element, relative to the same photospheric ratio. Observed FIP bias values typically vary between 1 and 4 (e.g., Baker et al. 2013; Del Zanna 2013) but higher values of up to 8 have also been reported (e.g., Widing & Feldman 2001).

Various processes have been proposed to be responsible for this effect, such as diffusion or inefficient Coulomb drag (e.g., von Steiger & Geiss 1989; Marsch et al. 1995; Pucci et al. 2010; Bø et al. 2013), thermoelectric driving (Antiochos 1994), chromospheric reconnection (Arge & Mullan 1998) and ion

cyclotron wave heating (Schwadron et al. 1999). Among the many candidates, a collisionless wave–particle mechanism based on the ponderomotive force (Laming 2004, 2015) appears to be able to describe this phenomenon more realistically than previously suggested mechanisms. The ponderomotive force arises as the reaction of the plasma to the refraction of Alfvén waves in the chromosphere and only acts on charged particles. In the chromosphere, low-FIP elements are predominantly ionized (ionization fraction $>99\%$; see Laming 2015, and references therein), while high-FIP elements are mostly neutral. Therefore, the ponderomotive force separates the low-FIP ions from the high-FIP neutrals by preferentially transporting them upwards to the corona. The result can then be observed as enhanced abundances of low-FIP elements in the corona compared to the photosphere. This is interesting because it places the fractionation closer to the beginning of the chain of events that lead to coronal heating, rather than being at the endpoint of the thermalization of that energy as would be the case for some of the diffusion-based mechanisms. Numerical simulations by Dahlburg et al. (2016) support the presence of the ponderomotive acceleration in solar coronal loops, with the appropriate magnitude and direction, and suggest it is a "by-product" of coronal heating. Recent work by Baker et al. (2021), Murabito et al. (2021), and Stangalini et al. (2021) found magnetic fluctuations in the chromosphere being magnetically connected to regions of high FIP bias in the corona, which supports this theoretical model. More recent numerical

simulations by Réville et al. (2021) using a shell turbulence model found that, under the assumption that turbulence is the main driver of coronal heating and solar wind acceleration, a ponderomotive force can appear in the chromosphere and the transition region, and can be strong enough to create the FIP effect. Martínez-Sykora et al. (2023) use a combination of observations from the IRIS mission (De Pontieu et al. 2014) and a 2.5D radiative magnetohydrodynamics model of the solar atmosphere to investigate the multifluid effects on the ponderomotive force associated with Alfvén waves.

The strongest FIP bias is typically observed in active regions. There are large variations in the measured FIP bias among active regions (Brooks et al. 2015; Mihailescu et al. 2022), and the overall FIP bias values observed in an active region also vary with time as the active region goes through the different stages that make up its lifetime. Previous studies found that emerging flux carries plasma with photospheric composition, i.e., FIP bias of approximately 1, at first (Widing & Feldman 2001). Then it increases with time in the emergence phase (Widing & Feldman 2001) and early decay phase (Baker et al. 2018), suggesting that the higher level of magnetic activity observed during the emergence phase is linked to the processes that drive the FIP effect. After an active region enters its decay phase, the FIP bias starts to decrease (Baker et al. 2015; Ko et al. 2016) until it reaches the FIP bias of the surrounding quiet Sun (Ko et al. 2016).

In addition, FIP bias values within an active region show a broad distribution (Mihailescu et al. 2022), indicating that processes acting on sub-active region scales can influence the FIP bias in different ways. For example, Baker et al. (2013) found that the FIP bias is highest at the loop footpoints and shows a mild enhancement along some of the active region loops. The same study also found that photospheric reconnection that manifests as photospheric flux cancellation and subsequent formation of a flux rope leads to FIP bias values closer to 1. This makes plasma composition a powerful tool for obtaining insight into the magnetic configuration and formation history of solar structures (see, e.g., Fletcher & Lopez Fuentes 2001; James et al. 2017; Baker et al. 2022).

The measured FIP bias values can also vary depending on the diagnostic used to measure it. While elements are broadly categorised into low-FIP and high-FIP, different low-FIP elements can show different levels of enhancement, and high-FIP elements can in some instances show enhancement too. The clearest example is S (FIP = 10.36 eV), which sits close to the boundary between low-FIP and high-FIP elements. In some instances it shows no or little enhancement (i.e., it behaves like a high-FIP element), while in others it shows significant enhancement (i.e., it behaves like a low-FIP element; see, e.g., the coronal hole measurements of Brooks & Warren 2011). In addition, in the EUV, FIP bias diagnostics also have an associated temperature given by the contribution functions of the lines used. For example, the Si X 258.38 Å/S X 264.22 Å diagnostic captures cooler coronal plasma as the formation temperature of the lines involved is around 1.5 MK, while the Ca XIV 193.87 Å/Ar XIV 194.40 Å diagnostic captures hotter coronal plasma since the lines involved form at around 4 MK. Therefore, differences in FIP bias values measured with different diagnostics can be due to either the elements themselves behaving differently or the diagnostic probing plasma at different temperatures. Ko et al. (2016) found a high correlation (correlation coefficient varying between 0.76 and
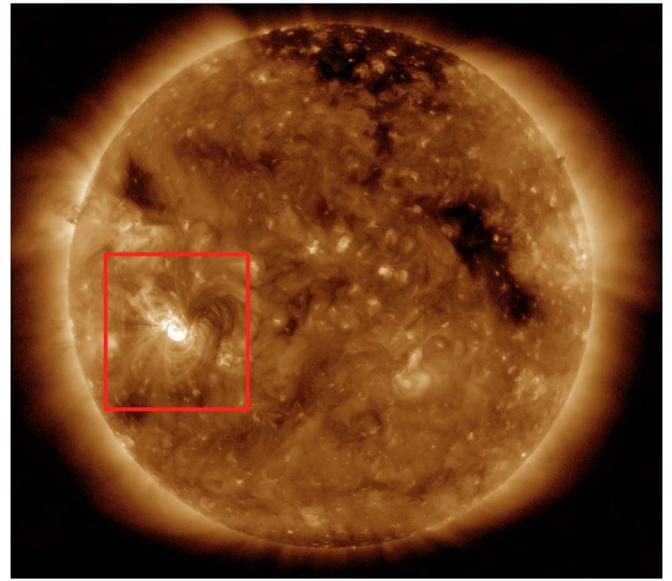
Figure 1. SDO AIA 193 Å context image of target AR 12665 on 2017 July 9 at 03:59 UT.

0.91 depending on the region selected) between the FIP bias measured with Si X 258.38 Å/S X 264.22 Å and Fe XII 195.12 Å/S X 264.22 Å ($\log(T_{\mathrm{MAX}}/\mathrm{K}) = 6.2$) in a decaying active region. This indicates that Fe and Si show similar FIP enhancement relative to S (note that S is the high-FIP element in both diagnostics). To et al. (2021) found more significant differences between FIP bias diagnostics when analyzing the Si X 258.38 Å/S X 264.22 Å compared to Ca XIV 193.87 Å/Ar XIV 194.40 Å FIP bias values in a small flare. This study suggests that the elements considered to be high-FIP could be behaving differently, i.e., S could be acting like a low-FIP element, as previously suggested by Laming et al. (2019). However, the conditions under which this phenomenon can happen are not yet fully understood.

This work investigates strikingly different fractionation patterns in different parts of an active region, again involving variations in the behavior of S. We use a combination of two FIP bias diagnostics characterizing the two fractionation patterns and simulations with the ponderomotive force model to further investigate mechanisms that could be responsible for the observed differences. Section 2 presents the photospheric and coronal evolution of the active region in the time leading up to the plasma composition observations. Section 3 describes these observations and the method for obtaining the FIP bias measurements. Section 4 presents the results of the simulation in the ponderomotive force model (Laming 2004, 2015) and how they can contribute to understanding the plasma composition observations. Finally, Section 5 provides a summary and discussion of the results in this study.

2. Evolution of AR 12665

2.1. White-light Continuum and Photospheric Magnetic Field Evolution

NOAA AR 12665 (see Figure 1) was first observed by the Solar Dynamics Observatory (SDO; Pesnell et al. 2012) Helioseismic and Magnetic Imager (HMI; Scherrer et al. 2012; Schou et al. 2012) at the eastern limb on 2017 July 5, with sunspots already present in both polarities. A new episode
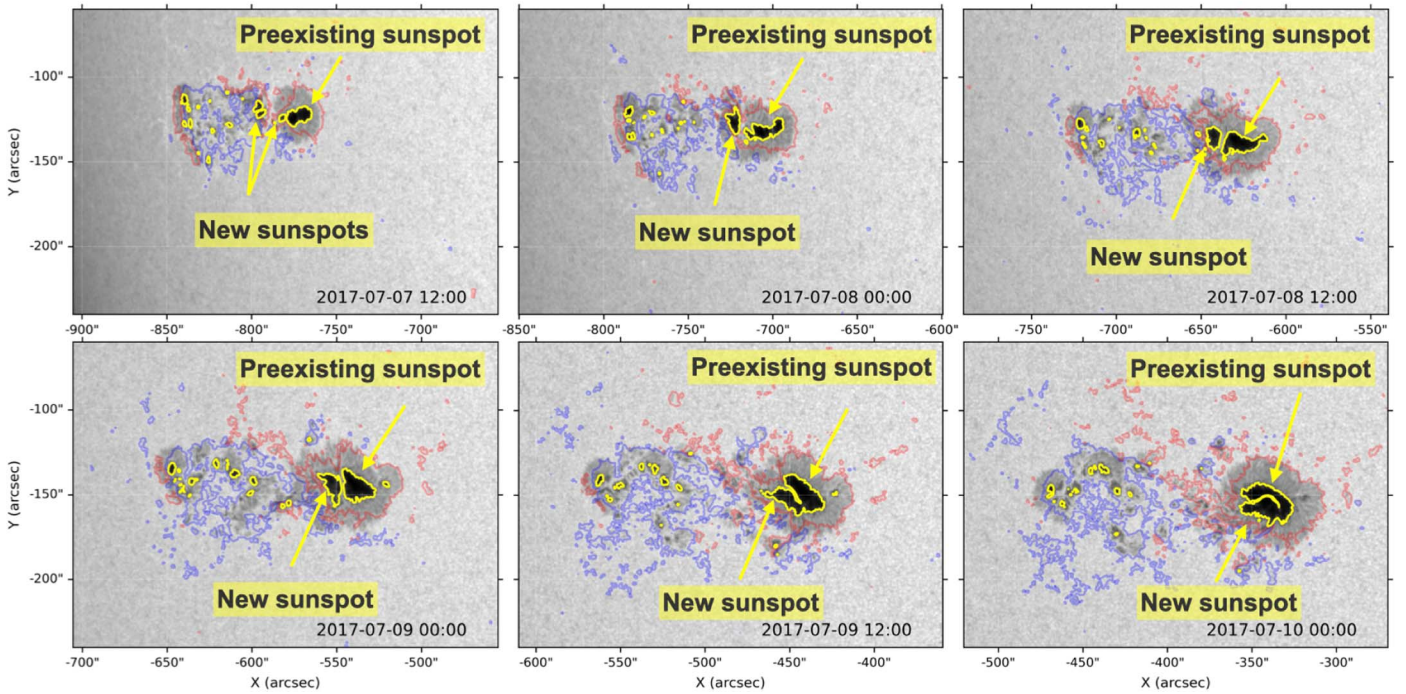
Figure 2. SDO HMI continuum emission and photospheric magnetic field evolution of AR 12665, every 12 hours, prior to and during the Hinode/EIS scans. Red (blue) contours represent areas of HMI line-of-sight photospheric magnetic field strength above (below) 200 G (−200 G). Yellow contours represent values below 25,000 counts s^{-1} in the continuum emission, indicating the location of the sunspot umbrae.

of significant flux emergence had begun between the leading and following polarities just as the AR region rotated into Earth view. By July 8, the emerging flux formed a new positive sunspot, which started moving toward (see top panels in Figure 2) and then orbiting the preexisting leading sunspot in a counterclockwise direction (see bottom panels in Figure 2). They eventually collided around 12:00 UT on July 9 and became one sunspot consisting of two umbrae separated by a light bridge within one common penumbra. Approximately 1 day later the light bridge disappeared (not pictured). This orbiting motion lasted for multiple days and was studied in detail by James et al. (2020). For the first approximately 1.5 days, the light bridge constantly separated the new from the preexisting positive sunspot umbrae. This enabled us to track the evolution of the newer and older parts of the active region separately.

2.2. Coronal Evolution

In the EUV, images from the SDO Atmospheric Imaging Assembly (AIA; Lemen et al. 2012) showed two main loop populations, namely the new loops and the preexisting loops. The new loops had been formed recently by the flux emergence and were rooted in the newly formed positive sunspot (see Figure 2). They were bright, relatively small hot loops in the core of the active region (see Figure 3). The preexisting loops had been part of the active region since before the flux emerged and were rooted in the preexisting positive sunspot (see Figure 2). They were fainter, high-lying warm loops located in the southern part of the active region (see Figure 3).

In the few days running up to the EUV Imaging Spectrometer (EIS) scans on July 9 at 01:08 UT and 14:15 UT, the active region showed modest activity, with only one C1.0 flare on July 7 at 13:37 UT and one C3.4 flare on July 8 at 23:50 UT. On July 9, however, the flaring activity became

more intense, with one M1.3 flare at 03:09 UT and four C-class flares at 06:15 UT, 07:28 UT, 08:55 UT, and 11:44 UT being observed at the boundary between the new and the preexisting loop populations.

3. Plasma Composition

3.1. Hinode EIS Observations

The FIP bias was calculated using observations from the EIS instrument (Culhane et al. 2007) on Hinode (Kosugi et al. 2007). The EIS data set contains six scans of the active region over a period of approximately 13 hr. In this work, we analyze the first and the last scans in this series. Details of the EIS scans used are provided in Table 1.

3.2. Method

We used two line pair diagnostics: Si X 258.38 Å (low FIP, FIP = 8.25 eV) and S X 264.22 Å (high FIP, FIP = 10.36 eV), and Ca XIV 193.87 Å (low FIP, FIP = 6.11 eV) and Ar XIV 194.40 Å (high FIP, FIP = 15.76 eV). According to the CHIANTI database (Dere et al. 1997) version 10 (Del Zanna et al. 2021), the theoretical formation temperatures for the two diagnostics are different: the Si X 258.38 Å and S X 264.22 Å lines have a formation temperature of $\log(T_{MAX}/K) = 6.2$, while the Ca XIV 193.87 Å and Ar XIV 194.40 Å form at temperatures of $\log(T_{MAX}/K) = 6.7$ and $\log(T_{MAX}/K) = 6.6$ respectively. The lines involved in the two diagnostics were fitted using the Python EISPAC software (Weberg et al. 2023), and line ratios for each diagnostic were calculated in every pixel in the EIS rasters to obtain an approximation of the FIP bias (see second column in Figures 4 and 5).

Line ratios, however, are sensitive to temperature and density effects, so they only provide context. Corrected FIP bias measurements were also calculated in a few key locations.
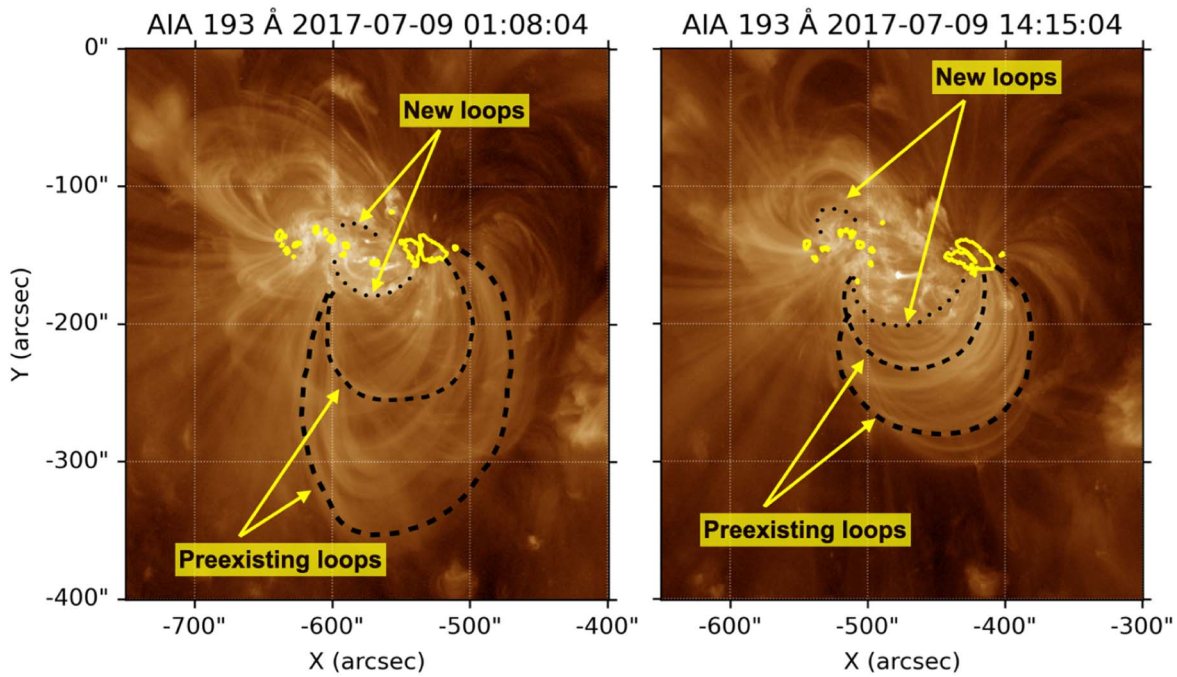
Figure 3. SDO AIA 193 Å passband images at the times matching the middle time of the EIS raster scans. Yellow contours represent values below 25,000 counts s^{-1} in the continuum emission, indicating the location of the sunspots. Black dotted (dashed) lines indicate representative examples of loops belonging to the new (preexisting) loop populations.

In these locations, spectra were averaged over multiple pixels (creating a macropixel) for all the lines included in the calculation. The method used for calculating the FIP bias in each of these macropixels uses a differential emission measure (DEM) to correct the temperature effects and a density analysis to correct for density effects. The DEM was derived using a series of Fe lines supplemented with a couple of Ca lines for additional high-temperature constraints (see Table 1), and the density was calculated using the Fe XIII 202.04 Å/Fe XIII 203.82 Å diagnostic. A Markov Chain Monte Carlo algorithm in the PintOfAle (Kashyap & Drake 1998, 2000) SolarSoft (Freeland & Handy 1998) package was used to compute the DEM distribution, and the CHIANTI database (Dere et al. 1997) version 10 (Del Zanna et al. 2021) to compute the contribution functions ($G(T, n)$) for each of the spectral lines involved in the diagnostic. We used the photospheric abundances of Scott et al. (2015a, 2015b). Note that using different sets of photospheric abundances could result in slightly different FIP bias measurements. This method is described in detail by Brooks & Warren (2011) and Brooks et al. (2015).

There are eight such locations in total. For each of the two rasters, four macropixels were selected: one for each loop population and each diagnostic (see first panel of Figures 4 and 5). This was done to obtain representative FIP bias values for each of the loop populations in both diagnostics. Slightly different macropixels were chosen for the two diagnostics. This is because the formation temperatures for the lines involved in the two diagnostics are different. For each diagnostic, the macropixels were chosen such that emission in the lines involved in the diagnostic is maximized.

3.3. Results

The FIP bias values are summarized in Table 2. In the emerging loops, the Si/S FIP bias increases with time from 2.3

to 3.0 and the Ca/Ar FIP bias from 2.6 to 3.3. This result agrees with previous studies, which found increasing FIP bias in the emergence phase of an active region (Widing & Feldman 2001; Baker et al. 2018). While the increase is observed in both diagnostics, the Ca/Ar values are slightly higher than the Si/S ones (albeit close to the 0.3 uncertainty in the measurements previously estimated by Brooks et al. 2017).

In the preexisting loops, the FIP bias behaves differently. The Si/S FIP bias changes slightly from 1.8 to 2.0, but this is within the 0.3 error limit. The Ca/Ar FIP bias shows an increase from 4.3 to 7.8 and, more importantly, shows consistently high values. This is very interesting because these values are significantly higher than the Si/S FIP bias values in the same loop population. To check that these high values are indeed representative of the entire population of preexisting loops, we examine the line ratio maps (see second column of Figure 5). The line ratio maps show high values everywhere in the population of preexisting loops, suggesting that the high FIP bias values are not isolated to the location of the macropixels that were chosen for the FIP bias calculation. Of course, we must be cautious when analyzing line ratio maps as they are sensitive to temperature and density effects. In particular, for the Ca/Ar line ratio, significant temperature effects due to plasma above $\log(T/K) = 6.6$ must be considered (see, e.g., Feldman et al. 2009; Doschek & Warren 2017; To et al. 2021). The DEM analysis (see third and fourth panels in Figures 4 and 5) shows that the emission in these preexisting loops is mostly cooler, with most of the emission coming from the $\log(T/K) = 6.2$–6.4 and $\log(T/K) = 6.4$–6.6 temperature bins, making it unlikely that the high values we see are a temperature effect.

The large Ca/Ar FIP bias values observed in the preexisting loops are not common, but similarly high values have been observed before, for example, in the Ca/Ar ratio in postflare loops (Doschek et al. 2018), in the Mg/Ne ratio in an emerging

Table 1
Summary of Hinode/EIS Study Details and Emission Lines Used for Creating the FIP Bias Measurements

EIS Study Details	
Raster middle times	09/07/2017 01:08 09/07/2017 14:15
Study acronym	DHB_007
Study number	544
Field of view	$492'' \times 512''$
Rastering	$2''$ slit, 123 positions, $4''$ coarse step
Exposure time	30 s
Total raster time	$1^\mathrm{h}1^\mathrm{m}30^\mathrm{s}$
Reference spectral window	Fe XII 195.12 Å
DEM lines	Fe VIII 185.213 Å, Fe VIII 186.601 Å, Fe IX 188.497 Å, Fe IX 197.862 Å, Fe X 184.536 Å, Fe XI 188.216 Å, Fe XI 188. 299 Å, Fe XII 192.394 Å, Fe XII 195.119 Å, Fe XIII 202.044 Å, Fe XIII 203.826 Å, Fe XIV 264.787 Å, Fe XIV 270.519 Å, Fe XV 284.16 Å, Fe XVI 262.984 Å, Ca XIV 193.874 Å, Ca XV 200.972 Å.
Density diagnostic lines	Fe XIII 202.04 Å, Fe XIII 203.82 Å
Line ratio lines	Si X 258.38 Å, S X 264.22 Å, Ca XIV 193.87 Å, Ar XIV 194.40 Å

flux region (Young & Mason 1997; Widing & Feldman 2001), in the Mg/O ratio in coronal mass ejection cores (Landi et al. 2010), and in various diagnostics in post-coronal mass ejection current sheets (Ciaravella et al. 2002; Ko et al. 2003). The newest aspect of the present results is the different behavior of the two diagnostics used to probe the plasma composition in the two loop populations. While in the emerging loops, the Si/S and Ca/Ar diagnostics indicate similar FIP bias values, in the preexisting loops there is a significant difference between the lower Si/S FIP bias values and higher Ca/Ar FIP bias values. This raises the question of whether the mechanism driving the FIP effect has different characteristics in the two loop populations, so this possibility was explored further using simulations from the ponderomotive force model.

4. The Ponderomotive Force Model

The ponderomotive force model (Laming 2004, 2015) is a 1D static model that proposes that the FIP effect is generated in the chromosphere by Alfvén wave activity originating in the corona. At coronal loop footpoints, refraction of these Alfvén waves in the high density gradient of the chromosphere (see Figure 6(a)) generates a ponderomotive force. This ponderomotive force acts on the ionized material (i.e., mostly low-FIP elements since they have a much higher ionization fraction than the high-FIP elements; see Figures 6(b) and (c)), preferentially bringing them upwards to the top of the transition region. Once plasma reaches the transition region, two things happen: (1) the temperature increases enough to ionize all elements, so low-FIP and high-FIP elements are no longer separated into ions and neutrals, and (2) there is no significant density gradient anymore, so the ponderomotive force disappears. This means that the fractionation process stops at the top of the transition region, and the fractionation pattern is locked in. From here, the fractionated plasma is transported up into the corona through other mechanisms. Note that the current implementation of the ponderomotive force model uses a 1D static model chromosphere, and so it does not cover this last part of the chain.

The pattern and strength of the fractionation process depend on the height in the chromosphere at which the ponderomotive force is generated. This, in turn, is dictated by whether the Alfvén wave driver is in resonance with the loop or not. Resonance here means that the wave travel time from one loop footpoint to the other is an integral number of wave half-periods. Resonant waves accumulate much more wave energy in the corona than in the chromospheric footpoints, and drive

the ponderomotive force close to the top of the chromosphere (see Figure 6(e)). This results in mild fractionation levels (see Figure 6(f)) because of the ionized background gas. Non-resonant waves drive the ponderomotive force at lower heights (see Figure 6(h)), which results in stronger fractionation levels (see Figure 6(i)) because the background gas is neutral.

4.1. Model Simulations

We use the ponderomotive force model to make predictions of the fractionation patterns in the two loop populations shown in Figures 4 and 5. We find that the simulation predictions match best with the Hinode EIS observations when assuming the driver is resonant waves in the emerging loops and nonresonant waves in the preexisting loops. This scenario is described in detail below.

We first estimate the resonant frequency of the emerging loops using the following parameters: loop length, plasma density along the loop, and magnetic field strength. The loop lengths were estimated using a potential field source surface (PFSS) model (IDL SolarSoft package provided by Schrijver & DeRosa 2003) of the active region. In the PFSS model, a representative loop was selected for each loop population and its length was calculated. The plasma density along the loop was measured in the macropixel boxes shown in Figures 4 and 5 using the Fe XIII 202.04 Å/Fe XIII 203.82 Å diagnostic from Hinode EIS. The photospheric magnetic field strength was measured using SDO HMI. All loop parameters are summarized in Table 3. The resonant frequency is given approximately by

$$f_{\mathrm{resonance}} = \frac{v_{\mathrm{A}}}{2L}, \tag{1}$$

where L is the loop length and v_{A} is the Alfvén speed calculated as

$$v_{\mathrm{A}} = \frac{B}{\sqrt{4\pi\rho}}, \tag{2}$$

where B is the coronal magnetic field strength and ρ is the loop density. We construct loop models matching the parameters in Table 3, where the 0–2500 km portions at each end of the loop are taken to be the chromospheric part of the loop, with the chromospheric model given by Avrett & Loeser (2008). The loop resonant frequencies are taken from calculations of the Alfvén wave propagation and by identifying the frequency at
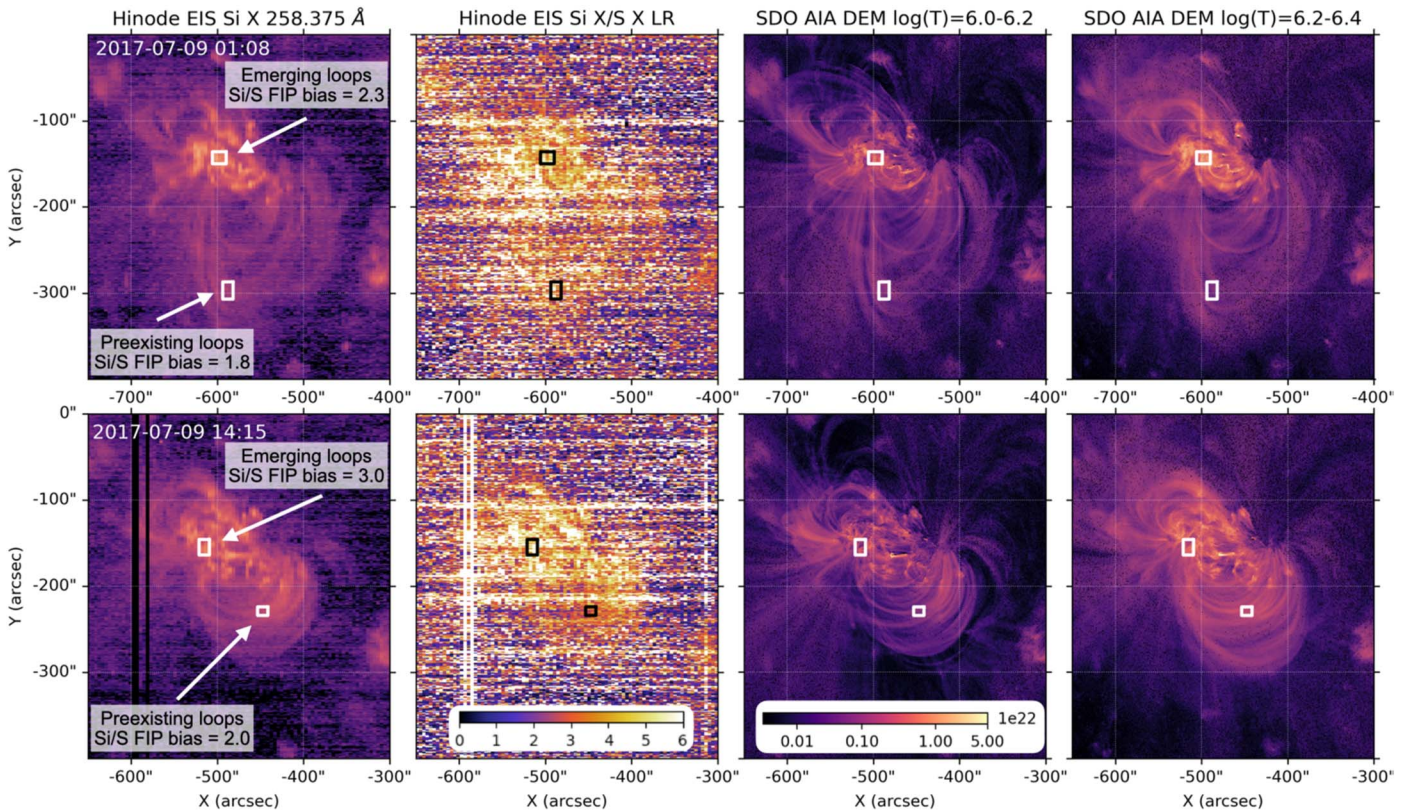
Figure 4. Si X/S X results. From left to right: Hinode EIS Si X 258.38 Å intensity, Hinode EIS Si X 258.38 Å/S X 264.22 Å line ratio, SDO AIA DEM in the $\log(T/K) = 6.0$–6.2 and the $\log(T/K) = 6.2$–6.4 temperature bins (computed using the method developed by Hannah & Kontar 2012, 2013). The boxes indicate the locations of the macropixels for this diagnostic.

which wave transmission from the chromosphere into the corona is maximized.

We estimated the resonance angular frequency of the emerging loops to be $\Omega_{\rm EL\ resonance} = 0.351$ rad s^{-1}. We then ran the model simulations assuming the fractionation process is driven by Alfvén waves at this frequency in both the emerging and the preexisting loops. This means at resonance with the emerging loops and off resonance with the preexisting ones. A discussion on why this is likely to be an appropriate choice is provided in Section 4.2.

Results for the resonant case are shown in Figures 6(d), (e), and (f). In this case, the ponderomotive acceleration starts to increase in the middle of the chromosphere and is highest at the top of it and in the transition region (Figure 6(e)). As a result, the abundances of Si and Ca (relative to H, i.e., absolute abundances) start increasing slightly from the middle of the chromosphere, and show the highest enhancement around the top of the chromosphere and in the transition region (Figure 6(f)). We focus on the predictions of relative abundance at the top of the transition region (i.e., 2500 km above the photosphere in these simulations) since the model suggests that abundance ratios are locked in once the plasma leaves this layer and is transported into the corona. Hence these are the ones to be compared with coronal observations. At the top of the transition region, Ar and S are essentially not fractionated. Ca and Si are both significantly fractionated. Ca shows a stronger fractionation than Si (Figure 6(f)), which is likely because the ionization fraction of Ca is higher than that of Si (Figure 6(b)), which means a larger fraction of the Ca atoms are affected by the ponderomotive force. This could

explain why the Hinode EIS observations show slightly higher Ca/Ar FIP bias values than Si/S FIP bias values in the emerging loops.

Results for the nonresonant case are shown in Figures 6(g), (h), and (i). In this case, the fractionation happens lower down in the chromosphere and is stronger overall: the ponderomotive acceleration starts increasing at the bottom of the chromosphere, reaches a maximum at the middle of the chromosphere, and then decreases (Figure 6(h)). The abundances of Si and Ca (relative to H) start increasing from the bottom of the chromosphere, which results in stronger enhancements at the top of the transition region compared to the resonant case. Interestingly, in this case S behaves similarly to Si and Ca rather than Ar: it becomes enhanced as well, but to a lesser degree than Si and Ca. As in the resonant case, Ar shows no fractionation. This could explain the strong difference between the Ca/Ar FIP bias and the Si/S FIP bias in the Hinode EIS measurements of the preexisting loops. As in the resonant case, Ca is more strongly enhanced than Si due to its higher ionization fraction. However, in the nonresonant case, the largest discrepancy between diagnostics comes from the fact that S experiences significant fractionation as well, i.e., it does not behave like a high-FIP element anymore. Therefore, the enhancement of Si is underestimated when measured relative to S.

It is important to note that the main free parameter when running the model and making predictions of FIP bias is the chromospheric amplitude $A_{\rm chromo}$ of the wave that drives the fractionation process. In the absence of observations that can help constrain the amplitudes of these waves at the chromospheric level, we need to make a guess for the amplitudes to be
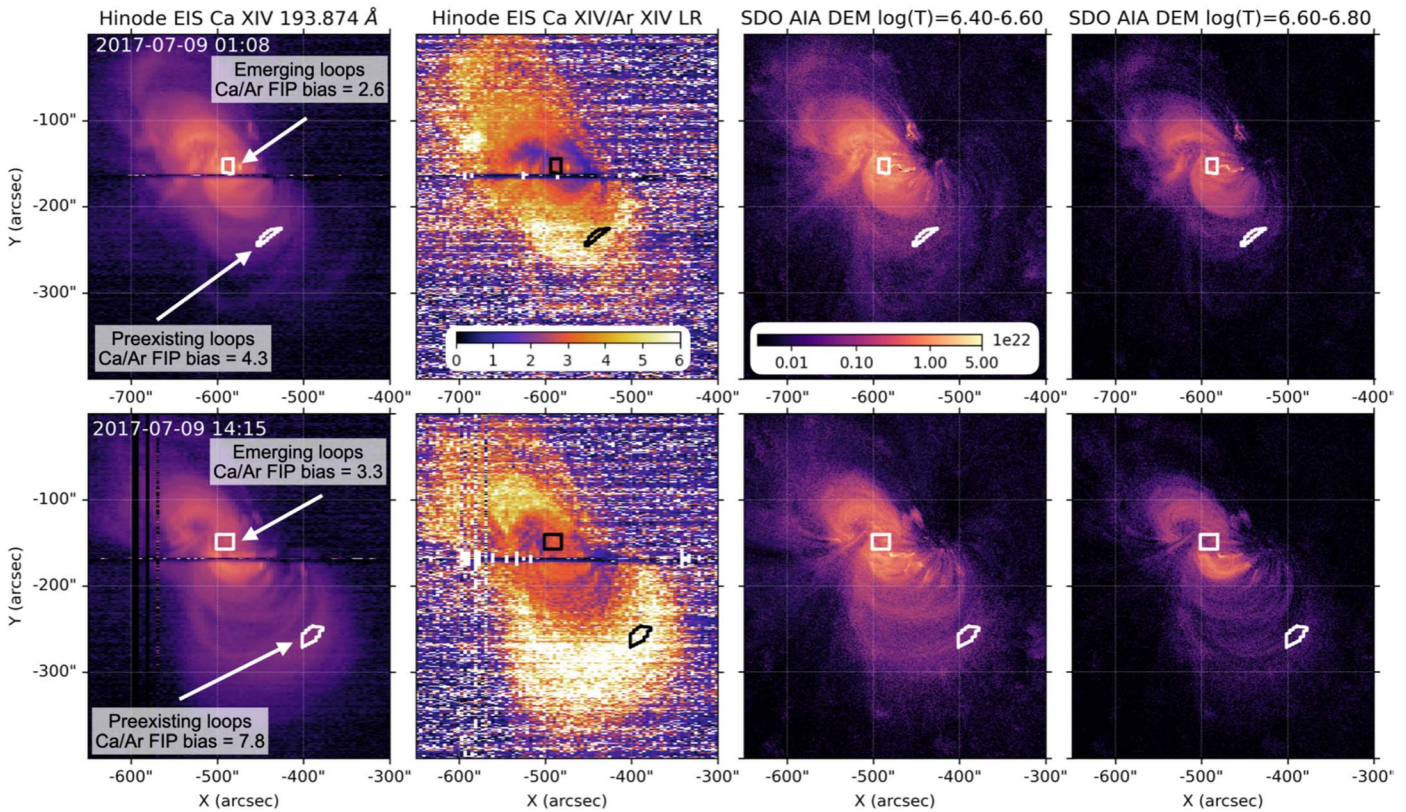
Figure 5. Ca XIV/Ar XIV results. From left to right: Hinode EIS Ca XIV 193.87 Å intensity, Hinode EIS Ca XIV 193.87 Å/Ar XIV 194.40 Å line ratio, SDO AIA DEM in the $\log(T/K) = 6.4$–6.6 and the $\log(T/K) = 6.6$–6.8 temperature bins (computed using the method developed by Hannah & Kontar 2012, 2013). The boxes indicate the locations of the macropixels for this diagnostic.

Table 2
Summary of Hinode/EIS FIP Bias Results

Raster Time	FIP Bias			
	Emerging Loops		Preexisting Loops	
	Si/S	Ca/Ar	Si/S	Ca/Ar
2017 July 9 01:08 UT	2.3	2.6	1.8	4.3
2017 July 9 14:15 UT	3.0	3.3	2.0	7.8

able to predict the FIP bias. Small changes in the wave amplitudes result in large changes in the estimated fractionation strength at the top of the transition region. However, while the strength of the fractionation is strongly dependent on the amplitude, the fractionation patterns for different elements mainly depend on the frequency of the wave driver (and, more specifically, on how close the frequency of the driver is to the resonant frequency of the loop) rather than the amplitude, so we can use the model predictions to obtain a qualitative understanding of the relative enhancement of different elements.

In the example described in this section and shown in Figure 6, we initiate the calculations with the wave amplitudes A_{chromo} given in Table 3. These are the input chromospheric wave amplitudes that resulted in fractionation patterns that best matched the Hinode EIS observations at 01:08 UT. The model predicts the waves to develop amplitudes A_{coronal} in the coronal portions of the loops. In the chromosphere, where the FIP fractionation is calculated, the resonant wave amplitude returns to $A_{\mathrm{chromo}} = 0.22$ km s^{-1}. The nonresonant wave amplitude is much larger, of the order of 1 km s^{-1}. This is characteristic of

the nonresonant waves, in that more wave energy accumulates in the chromosphere than in the corona.

Using the inputs listed in Table 3, the model predicts the following results: in the emerging loops (resonant wave driver case), an Si/S FIP bias of 1.8 and Ca/Ar FIP bias of 2.7, and in the preexisting loops (nonresonant wave driver case), an Si/S FIP bias of 1.5 and Ca/Ar FIP bias of 5.1. These values are directly calculated from the simulated composition patterns at the level of the transition region shown in Figures 6(f) and (i). Following the same approach, A_{chromo} can be changed slightly to obtain FIP bias values that match the Hinode EIS observations at 14:15 UT as well (see Table 4). The key result, however, is that, while the predicted FIP bias values depend on the selected A_{chromo}, the significant differences between the two diagnostics depend on whether the wave is resonant or not.

While one could model Si/S and Ca/Ar coming from different strands with different wave populations within each loop, we consider it a success that the same fractionation process (i.e., one wave in each loop, of the same frequency) for both Si/S and Ca/Ar reduces the former and increases the latter in going from emerging to preexisting loops. One might achieve better agreement between model and observation with more waves, but this would be at the expense of more model parameters.

4.2. Discussion of the Origin of Alfvén Waves

The simulations in the ponderomotive force model suggest that the fractionation pattern observed in the two loop populations could be explained if the driver is resonant waves
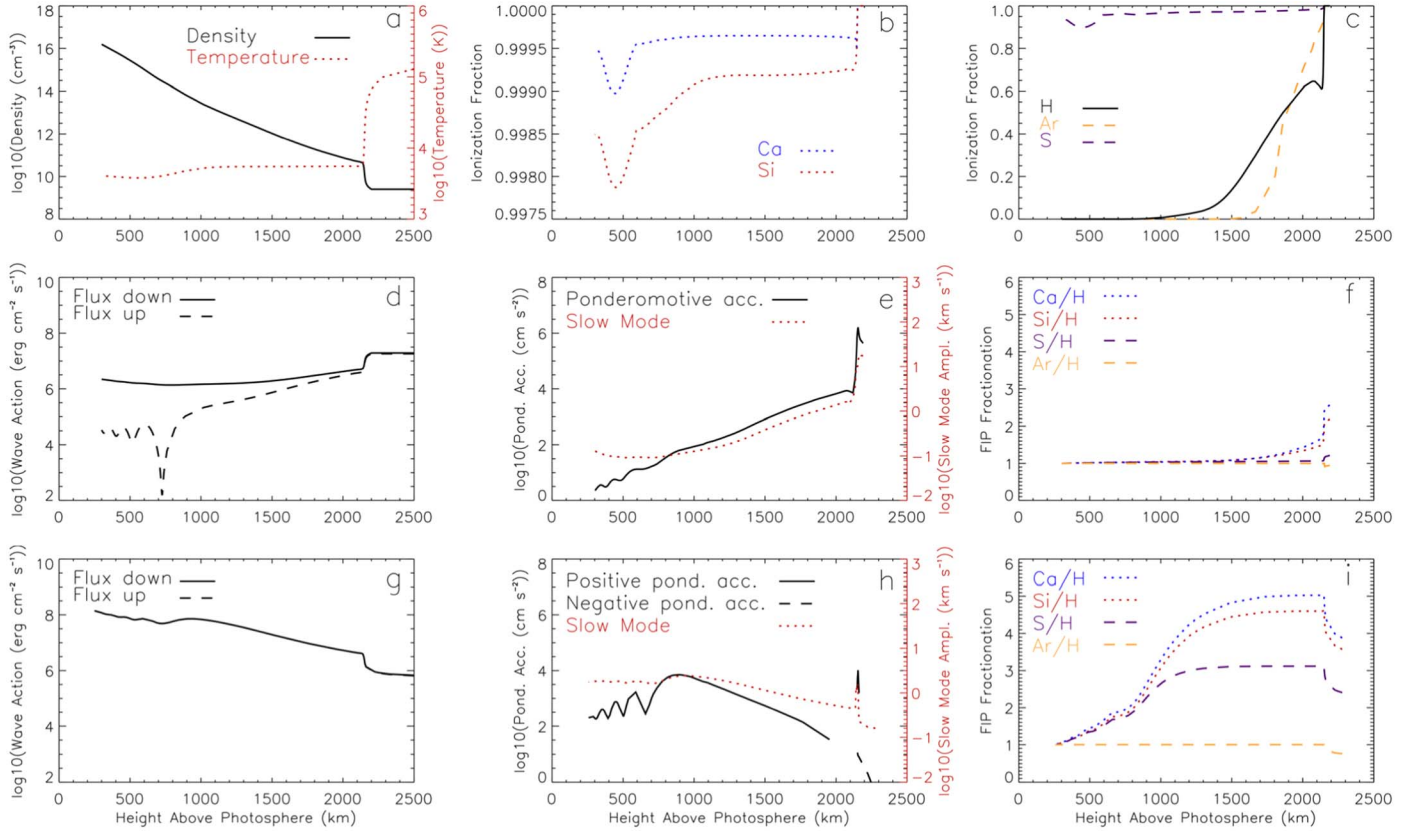
Figure 6. Predictions of the ponderomotive force model. The first row shows the variation with height of the following parameters: (a) electron temperature and density, (b) ionization fraction for low-FIP elements, and (c) ionization fraction for high-FIP elements. The second row shows the variation with height of (d) downward and upward fluxes of Alfvén wave energy for waves of assumed coronal origin, (e) ponderomotive acceleration, and (f) FIP bias relative to H in the case of resonant fractionation. The third row shows the variation with height of (g) fluxes of Alfvén wave energy—the downward and upward fluxes are identical, (h) ponderomotive acceleration, and (i) FIP bias relative to H in the case of nonresonant fractionation.

Table 3
Parameters Used for Predictions of the Ponderomotive Force Model

Parameter	Emerging Loops	Preexisting Loops
L	100 Mm	510 Mm
ρ	$10^{9.5}$ cm^{-3}	$10^{8.5}$ cm^{-3}
B	250 G	200 G
v_A	10^4 km s^{-1}	2.5×10^4 km s^{-1}
$f_{resonance}$	0.05 s^{-1}	0.025 s^{-1}
$\Omega_{resonance}$	0.351 rad s^{-1}	0.157 rad s^{-1}
A_{chromo}	0.22 km s^{-1}	0.03 km s^{-1}
$A_{coronal}$	44 km s^{-1}	14 km s^{-1}

Note. Parameters listed here follow the same notation as in Equations (1) and (2). For the wave amplitudes, A_{chromo} is the chromospheric wave amplitude at the $\beta = 1$ layer used as input for the model simulations and $A_{coronal}$ is the coronal wave amplitude predicted by the model.

Table 4
Predictions of the Ponderomotive Force Model with Variable A_{chromo}

Emerging Loops			Preexisting Loops		
A_{chromo}	Si/S	Ca/Ar	A_{chromo}	Si/S	Ca/Ar
0.20	1.61	2.31	0.025	1.32	3.13
0.22	1.80	2.70	0.03	1.48	5.1
0.26	2.22	4.00	0.035	1.68	7.0
0.30	2.87	6.1	0.04	1.93	14.7

Note. For the wave amplitudes, A_{chromo} is the chromospheric wave amplitude at the $\beta = 1$ layer. A_{corona} changes in proportion. Parameters are chosen to span the range of Si/S and Ca/Ar in Table 2.

in the emerging loops and nonresonant waves in the preexisting loops. This naturally raises a question regarding the origin of these waves. We propose that the waves giving rise to the fractionation seen in the emerging loops have a coronal driver, and consider both a coronal and a photospheric driver for the waves giving rise to the fractionation observed in the preexisting loops. The emerging loops make up the very active core of the active region, where nanoflares, for example, can give rise to coronal Alfvén waves that are naturally at resonance with the loop. The preexisting loops are less active,

which means an external driver is more likely to generate the waves needed for the fractionation.

The first candidate is of coronal origin. We speculate that resonant waves in the emerging loops could be communicated to the preexisting loops, where they will be nonresonant. To see this we write an equation of motion for waves on the preexisting loop (2) forced by kink oscillations of the emerging loop (1) with displacement x_2:

$$\rho_2(\ddot{x}_2 + \Omega_2^2 x_2) = -\frac{\partial}{\partial r}\left(\frac{\delta B_{\perp 1}^2}{8\pi} + \frac{B_0 \delta B_{\parallel 1}}{4\pi}\right). \quad (3)$$

Here we assume $\delta B_1 \propto 1/r$, where δB_1 is the magnetic field perturbation in emerging loop 1, with components

perpendicular and parallel to the ambient magnetic field B_0 indicated. The first Alfvénic term on the right-hand side is $\delta B_{\perp 1}^2/8\pi = \rho_1 \delta v_{\perp 1}^2/2$ and it oscillates at $2\Omega_1$ to give

$$\frac{x_2}{x_1} = \frac{\rho_1}{\rho_2}\frac{2\Omega_1^2}{\Omega_2^2 - 4\Omega_1^2}\frac{x_1}{R}, \tag{4}$$

where R is the separation between the flux tubes. With $x_1 = 44/0.351 = 125$ km, Equation (4) indicates that $x_2/x_1 = 0.3$ requires a separation between flux tubes of $2''$–$4''$, much smaller than the observed separation of order $100''$.

The effect of the second, compressive, term on the right-hand side is more model-dependent (e.g., Mikhalyaev & Solovév 2005; Verwichte et al. 2006). The r-component of the wavevector exterior to the emerging loop can be written when the plasma beta is $\beta \ll 1$ as

$$k_r^2 = \Omega^2 - k_z^2 v_{Ae}^2 = \frac{v_{A1}^2 - v_{Ae}^2}{1 + \rho_e/\rho_1}, \tag{5}$$

where $\Omega^2 = (B_e^2 + B_0^2)/[4\pi \times (\rho_e + \rho_1)]$ is the tube oscillation frequency in terms of exterior and interior ambient magnetic fields B_e, B_0, and densities ρ_e, ρ_1 (Mikhalyaev & Solovév 2005). When $v_{Ae} > v_{A1}$ (the usual case), k_r is imaginary and the exterior wave is evanescent, meaning that the kink oscillations are trapped inside the loop, making transfer of wave energy from one loop to the other unlikely. Such a situation has been studied in detail for magnetosonic waves escaping from reconnection current sheets by Provornikova et al. (2018). The foregoing is doubtless oversimplified, and many possibilities must exist for the excitation of wave modes as magnetic flux emerges. Waves generated by nanoflares, however, are highly localized to single loops rather than loop populations, which raises questions about whether this type of wave transfer could realistically take place.

A second candidate could be of photospheric origin, and include p- and g-mode oscillations or other perturbations of the photospheric plasma flows generated by the flux emergence in the close vicinity of the preexisting loop footpoints (see Figure 2). These can act as a driver for both resonant and nonresonant waves. Among the wide range of possible photospheric perturbations, those with long wavelengths could naturally couple and perturb the neighboring preexisting loop population at the same time. In this regard, it is worth noting that the global rotational motion seen in the active region suggests a photospheric or sub-photospheric driver on large spatial scales. Interestingly, Grant et al. (2022) have detected coherent waves across multiple pores in the photosphere, suggesting a coupled wave excitation mechanism and a driver acting on scales of several tens of megameters. The rotational motion observed in the active region studied here could also drive torsional Alfvén waves. The associated spatial scales of the driver may explain coupled behavior of different loops. The S enhancement in the preexisting loops (as suggested by the Hinode EIS observations) and the fact that, as suggested by the model, the fractionation process takes place lower down in the chromosphere in the nonresonant case support the scenario of a photospheric origin for the waves driving fractionation in the preexisting loops. It is important to note, however, that the low frequencies and long wavelengths implied for 3 or 5 minute p-modes that make them reflect more easily in the chromosphere mean that high chromospheric wave amplitudes of $>10\,\mathrm{km\,s^{-1}}$

are required. Higher-frequency nonresonant waves, such as modeled in Figure 6, reduce this amplitude to $\sim 1\,\mathrm{km\,s^{-1}}$.

These are a couple of options that could explain the presence of nonresonant waves in the preexisting loop. However, understanding the exact origin of these waves is beyond the scope of this work and should be investigated in depth in a separate study.

5. Summary and Discussion

Spectral analysis of Hinode EIS observations of NOAA AR 12665 shows very different FIP bias values in two parts of the active region. The emerging loops, i.e., the new part of the active region, show enhanced Si/S FIP bias (2.3–3.0) and slightly higher Ca/Ar FIP bias (2.6–3.3). The preexisting loops, i.e., the old part of the active region, show more modest Si/S FIP bias (1.8–2.0) but very strong Ca/Ar FIP bias (4.3–7.8). The Ca/Ar FIP bias is slightly higher than the Si/S FIP bias in the emerging loops, but much higher than the Si/S FIP in the preexisting loops. We find that the ponderomotive force model is able to predict this effect using simple assumptions about the properties of the waves driving the fractionation process in the two loops.

We propose that the fractionation pattern observed in the emerging loops can be produced by resonant Alfvén waves of coronal origin. In this case, Ar and S show no fractionation, while Ca and Si show significant fractionation (Ca slightly higher than Si, which could explain the slightly stronger Ca/Ar FIP bias compared to Si/S FIP bias). This can be explained by fractionation occurring at the top of the chromosphere (as was previously suggested for the hot core loops from measurements of significantly higher FIP bias values by Brooks & Yardley 2021).

The fractionation pattern observed in the preexisting loops can be produced by nonresonant waves. In this case, Ca and Si show stronger fractionation than in the previous case (Ca again slightly higher than Si) and Ar again shows no fractionation. The key difference is that, in these conditions, S shows significant fractionation as well, resulting in a much lower Si/S FIP bias than Ca/Ar FIP bias. This can be explained by fractionation occurring lower down in the chromosphere (as was previously suggested by Laming et al. 2019). Note that although the two diagnostics measure different FIP bias levels, they are both detecting coronal abundances in both the hot core loops and preexisting loops. It is the combination of Si/S and Ca/Ar FIP bias measurements that allows further probing of the model predictions and the development of the resonant/nonresonant wave explanation of the wider loop environment.

It is important to note that the model is only analyzing the environment of the chromosphere and transition region, and predicting abundances at the top of the transition region. Transport mechanisms from the top of the transition region to the corona must be considered to be able to make a prediction of the FIP bias in the corona. The model suggests that the change in abundance at the top of the transition region can be reached within minutes (Laming 2015). However, previous studies (Widing & Feldman 2001; Baker et al. 2018) found that the FIP bias increases with time in the emergence phase over hours to days. This indicates that transport processes that bring the fractionated plasma into the corona are much slower than the processes that drive the fractionation, so predicted chromospheric abundances will not be reflected in the corona right away. Nevertheless, assuming that these timescales for

coronal transport are similar in the emerging and preexisting loops, we can compare qualitative trends predicted by the ponderomotive force model to our Hinode EIS observations.

We observe an increase in both the Si/S FIP bias and the Ca/Ar FIP bias of the emerging loops over the 13 hr period between the two Hinode EIS scans. This could indicate that the fractionated plasma is slowly being transported to the corona, i.e., the fractionation pattern at the top of the transition region is slowly being reflected in the corona. The strong increase in the Ca/Ar FIP bias in the preexisting loops over the 13 hr period could be explained following the same reasoning, with the exception that the final Ca/Ar FIP bias is higher so the increase appears to be more drastic. The assumption of a steady increase requires reasonably quiet coronal conditions. However, we observe one M-class and four C-class flares occurring at the boundary between these two loop populations in between the first and the second Hinode EIS scans. In the EUV, previous studies showed that flaring can either temporarily reduce the FIP bias to photospheric values (Warren 2014) or increase it (To et al. 2021). While the boxes selected for our FIP bias measurements are located further away from the flaring sites, we cannot exclude the possibility that the flaring activity influences the coronal transport mechanisms in the loops we are studying.

Finally, this result is particularly relevant for connection science studies. Typically the FIP bias diagnostics used in remote sensing studies (e.g., Si/S, Fe/S, Ca/Ar, Mg/Ne) are different from the ones used for in situ measurements (e.g., Fe/O), so understanding when these diagnostics behave differently is important for connecting the two types of measurements. According to the ponderomotive force model, resonant waves drive little fractionation in larger loops (e.g., the ones in this study) and no fractionation in open loops (Laming 2015). However, as the present work suggests, fractionation can still be driven in these loops by nonresonant waves if an external driver is present. In this case the Si/S FIP bias would be very low (and this can be extended to other low-FIP elements relative to S) so the area under study could mistakenly be believed to show no/weak fractionation unless a second diagnostic (not including S) is used. Therefore, understanding what differences to expect between different FIP bias diagnostics and being able to predict in what conditions S starts experiencing significant fractionation are important for connecting in situ plasma parcels to their origin on the Sun. This is especially important given that S is commonly used in both remote sensing and in situ FIP bias diagnostics.

Acknowledgments

ORCID iDs

Teodora Mihailescu ⬥ https://orcid.org/0000-0001-8055-0472
David H. Brooks ⬥ https://orcid.org/0000-0002-2189-9313
J. Martin Laming ⬥ https://orcid.org/0000-0002-3362-7040
Deborah Baker ⬥ https://orcid.org/0000-0002-0665-2355
Lucie M. Green ⬥ https://orcid.org/0000-0002-0053-4876
Alexander W. James ⬥ https://orcid.org/0000-0001-7927-9291
David M. Long ⬥ https://orcid.org/0000-0003-3137-0277
Lidia van Driel-Gesztelyi ⬥ https://orcid.org/0000-0002-2943-5978
Marco Stangalini ⬥ https://orcid.org/0000-0002-5365-7546

References

Antiochos, S. K. 1994, AdSpR, 14, 139
Arge, C., & Mullan, D. 1998, SoPh, 182, 293
Asplund, M., Grevesse, N., Sauval, A. J., & Scott, P. 2009, ARA&A, 47, 481
Avrett, E. H., & Loeser, R. 2008, ApJS, 175, 229
Bø, I. M. Th., Esser, R., & Lie-Svendsen, Ø. 2013, ApJ, 769, 60
Baker, D., Brooks, D. H., Démoulin, P., et al. 2013, ApJ, 778, 69
Baker, D., Brooks, D. H., Démoulin, P., et al. 2015, ApJ, 802, 104
Baker, D., Brooks, D. H., van Driel-Gesztelyi, L., et al. 2018, ApJ, 856, 71
Baker, D., Green, L. M., Brooks, D. H., et al. 2022, ApJ, 924, 17
Baker, D., Stangalini, M., Valori, G., et al. 2021, ApJ, 907, 16
Brooks, D. H., Baker, D., Van Driel-Gesztelyi, L., & Warren, H. P. 2017, NatCo, 8, 183
Brooks, D. H., Ugarte-Urra, I., & Warren, H. P. 2015, NatCo, 6, 5947
Brooks, D. H., & Warren, H. P. 2011, ApJL, 727, L13
Brooks, D. H., & Yardley, S. L. 2021, SciA, 7, eabf0068
Ciaravella, A., Raymond, J. C., Li, J., et al. 2002, ApJ, 575, 1116
Culhane, J. L., Harra, L. K., James, A. M., et al. 2007, SoPh, 243, 19
Dahlburg, R. B., Laming, J. M., Taylor, B. D., & Obenschain, K. 2016, ApJ, 831, 160
De Pontieu, B., Title, A. M., Lemen, J. R., et al. 2014, SoPh, 289, 2733
Del Zanna, G. 2013, A&A, 558, A73
Del Zanna, G., Dere, K. P., Young, P. R., & Landi, E. 2021, ApJ, 909, 38
Dere, K. P., Landi, E., Mason, H. E., Monsignori Fossi, B. C., & Young, P. R. 1997, A&AS, 125, 149
Doschek, G. A., & Warren, H. P. 2017, ApJ, 844, 52
Doschek, G. A., Warren, H. P., Harra, L. K., et al. 2018, ApJ, 853, 178
Feldman, U., Warren, H. P., Brown, C. M., & Doschek, G. A. 2009, ApJ, 695, 36
Fletcher, L., Lopez Fuentes, M. C., Mandrini, C. H., et al. 2001, SoPh, 203, 255
Freeland, S. L., & Handy, B. N. 1998, SoPh, 182, 497
Grant, S. D. T., Jess, D. B., Stangalini, M., et al. 2022, ApJ, 938, 143
Hannah, I. G., & Kontar, E. P. 2012, A&A, 539, A146
Hannah, I. G., & Kontar, E. P. 2013, A&A, 553, A10
James, A. W., Green, L. M., Palmerio, E., et al. 2017, SoPh, 292, 71

James, A. W., Green, L. M., Van Driel-Gesztelyi, L., & Valori, G. 2020, A&A, 644, A137
Kashyap, V., & Drake, J. 2000, BASI, 28, 475
Kashyap, V., & Drake, J. J. 1998, ApJ, 503, 450
Ko, Y.-K., Raymond, J. C., Lin, J., et al. 2003, ApJ, 594, 1068
Ko, Y.-K., Young, P. R., Muglach, K., Warren, H. P., & Ugarte-Urra, I. 2016, ApJ, 826, 126
Kosugi, T., Matsuzaki, K., Sakao, T., et al. 2007, SoPh, 243, 3
Laming, J. M. 2004, ApJ, 614, 1063
Laming, J. M. 2015, LRSP, 12, 2
Laming, J. M., Vourlidas, A., Korendyke, C., et al. 2019, ApJ, 879, 124
Landi, E., Raymond, J. C., Miralles, M. P., & Hara, H. 2010, ApJ, 711, 75
Lemen, J. R., Title, A. M., Akin, D. J., et al. 2012, SoPh, 275, 17
Marsch, E., von Steiger, R., & Bochsler, P. 1995, A&A, 301, 261
Martínez-Sykora, J., Pontieu, B. D., Hansteen, V. H., et al. 2023, ApJ, 949, 112
Meyer, J.-P. 1985, ApJS, 57, 151
Mihailescu, T., Baker, D., Green, L. M., et al. 2022, ApJ, 933, 245
Mikhalyaev, B. B., & Solovév, A. A. 2005, SoPh, 227, 249
Murabito, M., Stangalini, M., Baker, D., et al. 2021, A&A, 656, A87

Pesnell, W. D., Thompson, B. J., & Chamberlin, P. C. 2012, SoPh, 275, 3
Provornikova, E., Laming, J. M., & Lukin, V. S. 2018, ApJ, 860, 138
Pucci, S., Lie-Svendsen, & Esser, R. 2010, ApJ, 709, 993
Réville, V., Rouillard, A. P, Velli, M., et al. 2021, FrASS, 8, 2
Scherrer, P. H., Schou, J., Bush, R. I., et al. 2012, SoPh, 275, 207
Schou, J., Scherrer, P. H., Bush, R. I., et al. 2012, SoPh, 275, 229
Schrijver, C. J., & DeRosa, M. L. 2003, SoPh, 212, 165
Schwadron, N. A., Fisk, L. A., & Zurbuchen, T. H. 1999, ApJ, 521, 859
Scott, P., Asplund, M., Grevesse, N., Bergemann, M., & Sauval, A. J. 2015a, A&A, 573, A26
Scott, P., Grevesse, N., Asplund, M., et al. 2015b, A&A, 573, A25
Stangalini, M., Baker, D., Valori, G., et al. 2021, RSPTA, 379, 20200216
To, A. S. H., Long, D. M., Baker, D., et al. 2021, ApJ, 911, 86
Verwichte, E., Foullon, C., & Nakariakov, V. M. 2006, A&A, 446, 1139
von Steiger, R., & Geiss, J. 1989, A&A, 225, 222
Warren, H. P. 2014, ApJL, 786, L2
Weberg, M. J., Warren, H. P., Crump, N., & Barnes, W. 2023, JOSS, 8, 4914
Widing, K. G., & Feldman, U. 2001, ApJ, 555, 426
Young, P. R., & Mason, H. E. 1997, SoPh, 175, 523